

Structural Origin of Shear Viscosity of Liquid Water

*Tsuyoshi Yamaguchi**

Graduate School of Engineering, Nagoya University, Furo-cho, Chikusa, Nagoya, Aichi 464-8603, Japan.

ABSTRACT

The relation between the microscopic structure and shear viscosity of liquid water was analyzed by calculating the cross correlation between the shear stress and the two-body density using molecular dynamics simulation. The slow viscoelastic relaxation that dominates the steady-state shear viscosity was ascribed to the destruction of the hydrogen-bonding network structure along the compression axis of the shear distortion, which resembles the structural change under isotropic hydrostatic compression. It means that the shear viscosity of liquid water reflects the anisotropic destruction-formation dynamics of the hydrogen-bonding network.

1. Introduction

Shear viscosity is one of the transport coefficients of liquids, which describes the current of transverse momentum.¹ Provided that it governs the macroscopic flow of liquids, it plays an essential role in treating flows in chemical engineering, mechanical engineering, geophysics, and other fields. In addition, the shear viscosity of a solvent is often regarded as a measure of the rates of dynamic processes of solutes dissolved in the solvent. It is therefore an important and interesting issue to understand the shear viscosity of liquids in terms of microscopic structure and intermolecular interaction.

We recently developed a theoretical formalism to extract the liquid structure and dynamics responsible for shear viscosity by evaluating the cross correlation function between the shear stress and the two-body density.² The formalism was applied to liquid methanol, and demonstrated the roles of the prepeak structure in viscoelastic relaxation. In this work, the same formalism was applied to liquid water to clarify the structural origin of its shear viscosity.

Liquid water is a popular solvent that is abundant on earth. There is no doubt of the crucial roles of water in biological processes.³ Its microscopic structure is characterized by the three-dimensional hydrogen-bonding network structure, and this peculiar structure is considered to affect various macroscopic properties of liquid water.⁴ It is well known that the shear viscosity of water shows characteristic dependence on both temperature and pressure, and its microscopic mechanism has long been studied intensively with various methods.^{5,6,7} Although the target of our present study is limited to water at the ambient condition, we believe it can be a first step to understand the anomalous behaviors of shear viscosity under various conditions.

2. Theoretical Formulation

According to the Kubo-Green formula, the steady-state shear viscosity of liquid, denoted as η_0 , is described in terms of the time correlation function of the anisotropic part of the stress tensor, $\mathbf{P}^{(s)}$, as^{8,9}

$$\eta_0 = \frac{V}{k_B T} \int_0^\infty dt \langle P_{xz}^{(s)}(0) P_{xz}^{(s)}(t) \rangle, \quad (1)$$

where k_B and T stand for the Boltzmann constant and the absolute temperature, respectively. Equation (1) states that the steady-state shear viscosity is determined by the dynamics of the stress tensor.

In order to examine the coupling between the dynamics of the stress tensor and the liquid structure, the cross correlation function between the shear stress and the two-body density at different times is defined as²

$$\rho_{\eta, \alpha\gamma}^{(2)}(|\mathbf{q}|, t) \equiv \frac{q^2}{q_x q_z} \langle \delta \rho_{\alpha\gamma}^{(2)}(\mathbf{q}, t) P_{xz}^{(s)} \rangle. \quad (2)$$

Here, the two-body density is defined as

$$\rho_{\alpha\gamma}^{(2)}(\mathbf{q}) \equiv \tilde{\rho}_\alpha^*(\mathbf{q}) \tilde{\rho}_\gamma(\mathbf{q}), \quad (3)$$

$$\delta \rho_{\alpha\gamma}^{(2)}(\mathbf{q}) \equiv \rho_{\alpha\gamma}^{(2)}(\mathbf{q}) - \langle \rho_{\alpha\gamma}^{(2)}(\mathbf{q}) \rangle, \quad (4)$$

where $\tilde{\rho}_\alpha(\mathbf{q})$ denotes the density field of the site α at the wavevector \mathbf{q} in the reciprocal space. The interaction-site description of the dynamics of molecular liquids is employed here, where the reorientational motion is described as the coupled diffusion of different sites.¹⁰ The interaction site refers to a real or united atom, and a water molecule is composed of one oxygen and two hydrogen sites, namely, O, H and H'. The trivial orientational dependence is factored out in the

definition of eq. (2) to define $\rho^{(2)}_{\eta,\alpha\gamma}(q,t)$ as a scalar function. According to the linear response theory, $\rho^{(2)}_{\eta,\alpha\gamma}(q,t)/k_B T$ is interpreted as the response of the two-body density to the shear deformation. The pure shear deformation is described as the superposition between the uniaxial compression and the uniaxial expansion. The structural responses along the compression and the expansion axes have the same amplitude and the opposite sign, and $\rho^{(2)}_{\eta,\alpha\gamma}(q,t)$ possesses the same sign as the change in the two-body density along the compression axis.

When the liquid is composed of monoatomic molecules, the initial value of $\rho^{(2)}_{\eta,\alpha\gamma}(q,t)$ is given by

$$\rho^{(2)}_{\eta,\alpha\gamma}(q, 0) = -k_B T q \frac{\partial}{\partial q} \chi_{\alpha\gamma}(q), \quad (5)$$

where the partial static structure factor $\chi_{\alpha\gamma}(q)$ is defined as

$$\chi_{\alpha\gamma}(|\mathbf{q}|) = \frac{1}{V} \langle \rho^{(2)}_{\alpha\gamma}(\mathbf{q}) \rangle. \quad (6)$$

Here, the volume of the system is denoted as V . Equation (5) indicates that the structure factor is compressed in a uniform way along the compression axis just after the instantaneous shear deformation.

The factorization approximation employed in the mode-coupling theory (MCT) gives an approximate expression for $\rho^{(2)}_{\eta,\alpha\gamma}(q,t)$ as

$$\rho^{(2)}_{\eta,\alpha\gamma}(q, t) \cong -k_B T q \left[\mathbf{F}(q, t) \cdot \frac{d\mathbf{c}(q)}{dq} \cdot \mathbf{F}(q, t) \right]_{\alpha\gamma}, \quad (7)$$

where bold symbols mean matrices whose indices refer to the interaction site, and the dot stands for the product of two matrices. The functions $F_{\alpha\gamma}(q,t)$ and $c_{\alpha\gamma}(q)$ denote the partial intermediate scattering function and the site-site direct correlation function,¹¹ respectively. Equation 7 relates the dynamic stress-structure coupling to the structural dynamics represented by the intermediate scattering function.

The coupling between the two-body density and the shear stress can also be defined in real space as

$$\rho_{\eta,\alpha\gamma}^{(2r)}(|\mathbf{r}|, t) \equiv \frac{r^2}{r_x r_z} \langle \delta \rho_{\alpha\gamma}^{(2r)}(\mathbf{r}, t) P_{xz}^{(s)} \rangle, \quad (8)$$

where the two-body density in the real space is given by

$$\rho_{\alpha\gamma}^{(2r)}(\mathbf{r}) \equiv \int d^3\mathbf{R} \rho_{\alpha}(\mathbf{R}) \rho_{\gamma}(\mathbf{R} + \mathbf{r}), \quad (9)$$

$$\delta \rho_{\alpha\gamma}^{(2r)}(\mathbf{r}) \equiv \rho_{\alpha\gamma}^{(2r)}(\mathbf{r}) - \langle \rho_{\alpha\gamma}^{(2r)}(\mathbf{r}) \rangle. \quad (10)$$

The density field of the site α in the real space is denoted as $\rho_{\alpha}(\mathbf{r})$ here. The average of $\rho_{\alpha\gamma}^{(2r)}(\mathbf{r})$ is related to the radial distribution function, $g_{\alpha\gamma}(r)$, as

$$\frac{1}{V} \langle \rho_{\alpha\gamma}^{(2r)}(\mathbf{r}) \rangle = \rho_{\alpha} \rho_{\gamma} [g_{\alpha\gamma}(|\mathbf{r}|) - 1] + \rho_{\alpha} \delta_{\alpha\gamma} \delta(\mathbf{r}), \quad (11)$$

where ρ_{α} stands for the number density of the site α . Since the two-body densities in the real and the reciprocal spaces, eqs. (3) and (9), are related to each other through the Fourier transformation, the similar relation also holds between $\rho_{\eta,\alpha\gamma}^{(2)}(q, t)$ and $\rho_{\eta,\alpha\gamma}^{(2r)}(r, t)$.

In the case of monoatomic liquids, the real space counterpart of eq. (4) is given by

$$\rho_{\eta,\alpha\gamma}^{(2r)}(r, 0) = \rho_{\alpha} \rho_{\gamma} k_B T r \frac{\partial}{\partial r} g_{\alpha\gamma}(r), \quad (12)$$

which also describes the uniform compression along the compression axis.

3. Computational Methods

Molecular dynamics (MD) simulation runs were performed on TIP4P/2005 model of water¹² at 300 K and 1 bar under NPT ensemble. We employed the TIP4P/2005 model because it has been shown to reproduce the shear viscosity of liquid water well. The Nosé-Hoover thermostat and

the Parrinello-Rahman barostat were used to control the temperature and the pressure of the system, respectively.¹³ The cubic cell was filled with 1728 water molecules, and the periodic boundary condition was applied. The length of the equilibration run was 100 ps, which was followed by the production run of 100 ns length. The simulation was performed using GROMACS 5.1.2 package.¹⁴ The equation of motion was integrated using the Verlet algorithm with the time step of 1 fs. The bond lengths and the bond angle of water were fixed with the SETTLE algorithm.¹⁵ The long-range part of the Coulombic interaction was evaluated by means of the Particle-Mesh-Ewald method with the Fourier spacing of 0.12 nm. The short-range parts of the intermolecular interactions were cut off at 1.1 nm. The stress tensor was calculated at every 2 step and recorded at every 100 step. The coordinates of all the atoms were recorded at every 1000 step. A short run of the recording interval of 10 steps, whose total length was 10 ns, was performed to evaluate the short-time parts of the correlation functions. All the five components of the shear stress tensor were used for the correlation functions eqs. (1), (2), and (8) based on the orientational symmetry of the system.

4. Results and Discussion

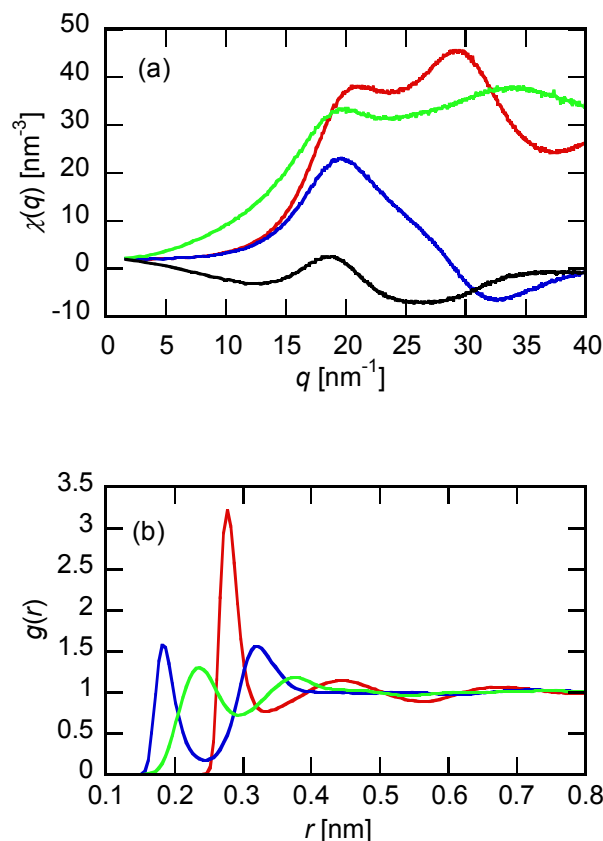


Figure 1. Site-site correlation functions describing the equilibrium structure of water are plotted. Panels (a) and (b) show the partial static structure factors and the site-site radial distribution functions, respectively. The O-O, O-H, and H-H components are shown with the red, blue, and green curves, respectively. The correlation between “different” H atoms are also shown with the black curve in panel (a).

Figure 1 shows the equilibrium structure of liquid water as a reference for the later analysis. A characteristic of the static structure factor of liquid water is the double-peak structure of $\chi_{\text{OO}}(q)$ with the peaks at 20 nm^{-1} and 30 nm^{-1} , respectively, which has been confirmed experimentally by X-ray scattering.¹⁶ The hydrogen-bonding structure is evident in the site-site radial distribution

functions. The peaks of $g_{\text{OH}}(r)$ at 0.19 nm and $g_{\text{OO}}(r)$ at 0.28 nm originate from the pair of water molecules interacting directly through a hydrogen bond. In addition, the second peak of $g_{\text{OO}}(r)$ at 0.45 nm represents the tetrahedral hydrogen-bonding network structure characteristic to water.

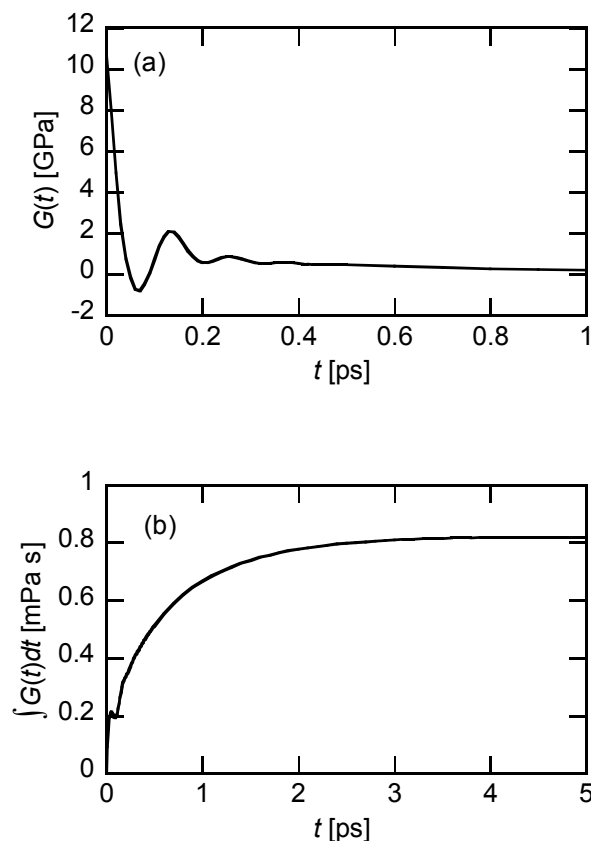


Figure 2. The autocorrelation function of the shear stress, $G(t)$, is shown. The short-time part is enlarged in panel (a), while the running integral is plotted in panel (b).

Figure 2 shows the time correlation function of the shear stress, $G(t)$, defined as

$$G(t) = \frac{V}{k_B T} \langle P_{xz}^{(s)}(0) P_{xz}^{(s)}(t) \rangle. \quad (13)$$

The time integration of $G(t)$ gives η_0 according to eq. (1). The fast oscillation within several hundreds of fs is followed by a slow tail in $G(t)$. The tail decays within 5 ps, and the value of η_0 is evaluated to be 0.82 mPa s. This value is close to the experimental one (0.89 mPa s at 298 K),

and it lies within the values reported by MD simulations using the same water model.^{7,17,18,19,20} The relaxation time of the slow tail was estimated to be 0.7 ps by fitting $G(t)$ at $t > 0.5$ ps to an exponential function. The relaxation time is close to the value determined from the depolarized Raman spectrum.^{21,22} The slow tail dominates the steady-state shear viscosity according to Fig. 2(b), which means that resolving the microscopic origin of the slow tail is essential to understand the shear viscosity of water at the molecular level.

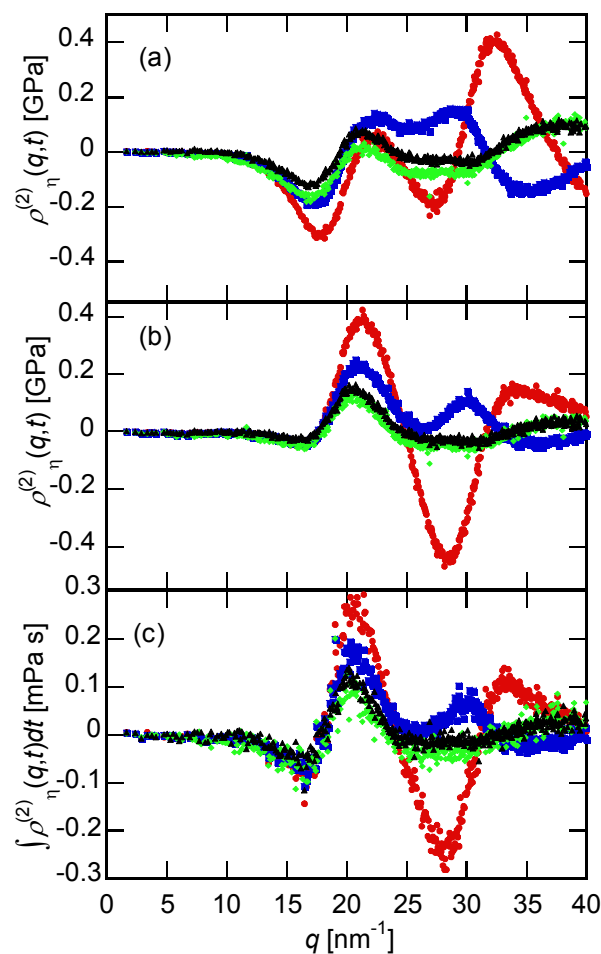


Figure 3. The cross correlation functions between the shear stress and the two-body density, $\rho^{(2)}_{\eta,\alpha\gamma}(q,t)$, are plotted as the functions of wavenumber, q . The O-O, O-H, and H-H components are shown with the red, blue, and green symbols, respectively, and the H-H' components are

with the black ones, where H-H' stands for the pair of different H-atoms. The correlation functions at $t = 0$ and 0.1 ps are shown in panels (a) and (b), respectively, and the profiles integrated over $0 < t < 5$ ps are in panel (c).

The cross correlation functions between the shear stress and the two-body density, $\rho^{(2)}_{\eta,\alpha\gamma}(q,t)$, are plotted in Fig. 3. The initial profiles in Fig. 3(a) resemble those predicted from the derivative of the static structure factor, $\chi_{\alpha\gamma}(q)$, for the uniform compression, eq. (5). The two-body density experiences the large structural rearrangement within 100 fs, as is shown in Fig. 3(b). The rearrangement is especially large for the O-O component.

The time-integrated profiles are shown in Fig. 3(c). The integration was truncated at $t = 5$ ps, because the integration of $G(t)$ converges within 5 ps as is exhibited in Fig. 2(b). The profiles in Fig. 3(c) corresponds to the change in the partial structure factor under steady-state shear flow. Comparing Figs. 3(b) and 3(c), it should be noticed that the profiles at $t = 100$ fs resemble the integrated ones. It means that the structural rearrangement does not occur in the slow tail region of $G(t)$ (Fig. 2(a)), and that the profiles in this time region dominate the integrated profiles.

The positive peak of $\rho^{(2)}_{\eta,\text{OO}}(q,t)$ at $q = 21 \text{ nm}^{-1}$ in Fig. 3(c) corresponds to the low- q peak of $\chi_{\text{OO}}(q)$, while the negative peak at $q = 28 \text{ nm}^{-1}$ does to the high- q peak. Under the steady-state shear flow, therefore, the low- q peak of the O-O component of the structure factor grows along the compression axis, whereas the high- q peak declines. This structural response to the shear flow actually resembles the change in the structure factor under the hydrostatic isotropic compression. The X-ray structure factor of liquid water, which mainly reflects $\chi_{\text{OO}}(q)$, has been determined experimentally as the function of hydrostatic pressure.¹⁶ The low- q peak is reported to grow with pressure, while the high- q peak diminishes. Therefore, the uniaxial compression of

the shear deformation induces the similar change in the microscopic structure of liquid water to the isotropic hydrostatic pressure.

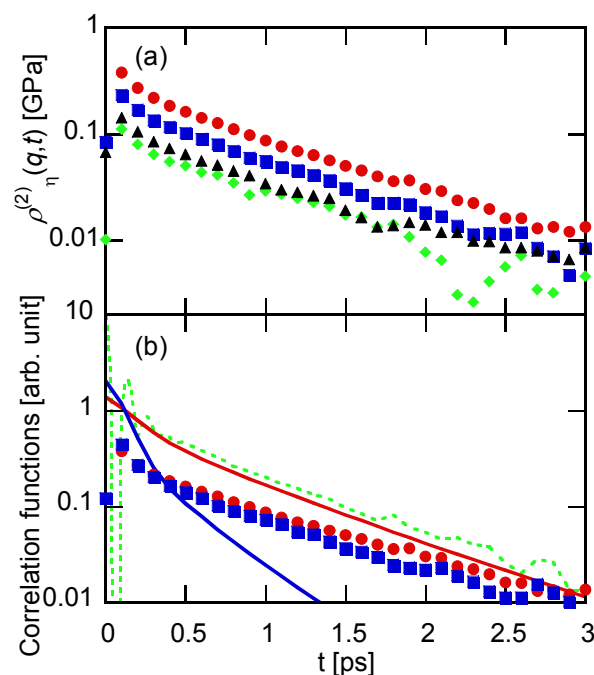


Figure 4. The time profiles of $\rho^{(2)}_{\eta,\alpha\gamma}(q,t)$ are plotted. The value of q is 21 nm^{-1} in panel (a). The O-O, O-H, and H-H components are shown with the red, blue, and green symbols, respectively, and the H-H' components are with the black ones, where H-H' stands for the pair of different H-atoms. In panel (b), $\rho^{(2)}_{\eta,OO}(q = 21.0 \text{ nm}^{-1}, t)$ (red circles) and $-\rho^{(2)}_{\eta,OO}(q = 28.5 \text{ nm}^{-1}, t)$ (blue squares) are compared with $G(t)$ (green dotted curve), $F^2_{OO}(q = 20.2 \text{ nm}^{-1}, t)$ (red solid curve), and $F^2_{OO}(q = 28.6 \text{ nm}^{-1}, t)$ (blue solid curve).

The dynamics of $\rho^{(2)}_{\eta,\alpha\gamma}(q,t)$ at the two peaks is shown in Fig. 4. The time profiles of the four components of $\rho^{(2)}_{\eta,\alpha\gamma}(q,t)$ at the positive peak, $q = 21.0 \text{ nm}^{-1}$, are compared with each other in Fig. 4(a). The short-time non-monotonic dynamics reflects the fast structural rearrangement as is observed between Figs. 3(a) and 3(b). The decays of these four components are close to each other, which indicates that the slow structural relaxation after the shear deformation is

independent of the atomic components. The dynamics of $\rho_{\eta,OO}^{(2)}(q,t)$ at the positive and negative peaks are compared in Fig. 4(b). The relaxation dynamics is independent also of the wavenumber q .

The relaxation dynamics of $\rho_{\eta,\alpha\gamma}^{(2)}(q,t)$ is also compared with other correlation functions. First, the relaxation of the tail of $G(t)$ is as slow as those of $\rho_{\eta,OO}^{(2)}(q,t)$ at the two peaks, which means that the slowest mode of the viscoelastic relaxation of water reflects the structural relaxation of these two modes.

According to the MCT-like approximation, eq. (7), the relaxation dynamics of $\rho_{\eta,\alpha\gamma}^{(2)}(q,t)$ is described by the square of the intermediate scattering function at the same wavenumber, $F_{\alpha\gamma}(q,t)$. In order to test the approximation, $F_{OO}^2(q,t)$ at the two peaks are compared with $\rho_{\eta,OO}^{(2)}(q,t)$ at the corresponding wavenumber in Fig. 4(b). $F_{OO}^2(q,t)$ at the low- q peak describes the slow relaxation of $\rho_{\eta,\alpha\gamma}^{(2)}(q,t)$ fairly well, whereas $F_{OO}^2(q,t)$ at the high- q peak relaxes faster. Therefore, the MCT-like approximation works at the low- q peak, while it fails at the high- q peak. The slowest mode of the shear relaxation reflects the relaxation of the intermediate scattering function at the low- q peak.

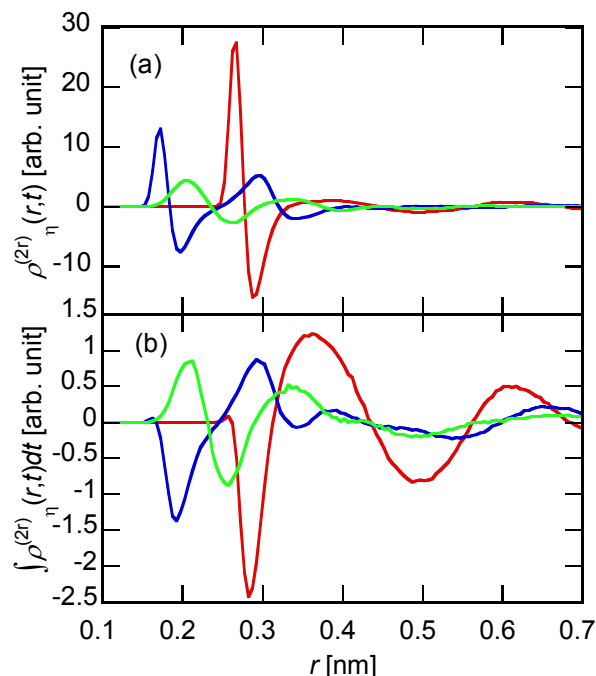


Figure 5. The cross correlation functions $\rho^{(2r)}_{\eta,\alpha\gamma}(r,t)$ are plotted as the functions of r . The O-O, O-H, and H-H components are drawn with the red, blue, and green curves, respectively. The initial responses, $t = 0$, are shown in panel (a), while the functions are integrated over $0 < t < 5$ ps in panel (b).

The real-space version of the cross-correlation function, $\rho^{(2r)}_{\eta,\alpha\gamma}(r,t)$, is shown in Fig. 5 to obtain more intuitive picture of the structural relaxation. The initial response in Fig. 5(a) is essentially explained as the uniform compression described by eq. (12). The profile demonstrates large rearrangement at $t < 100$ fs, although the result is not exhibited for brevity. The profile at $t = 100$ fs resembles the integrated one shown in Fig. 5(b), as is the case of $\rho^{(2)}_{\eta,\alpha\gamma}(q,t)$ in Fig. 3.

The O-O and O-H components of the time-integrated profiles in Fig. 5(b) show strongly negative peaks at the corresponding positions of the first peaks of the radial distribution functions in Fig. 1(b), respectively. The first peaks of $g_{\text{OO}}(r)$ at 0.28 nm and $g_{\text{OH}}(r)$ at 0.19 nm

originate in the pair of water molecules of direct hydrogen bond, and the negative peaks of $\rho^{(2r)}_{\eta,\alpha\gamma}(r,t)$ indicate that the direct hydrogen bond decreases along the compression axis of the shear deformation. In addition to the decrease in the direct hydrogen bond, the O-O component in Fig. 5(b) is negative at the position of the second peak of $g_{OO}(r)$, 0.45 nm, which means that the tetrahedral network structure is also destroyed along the compression axis. On the other hand, the O-O component shows a positive response at the first minimum of $g_{OO}(r)$, 0.35 nm, suggesting the increase in the interstitial water. In summary, the real-space profile of the time-integrated cross-correlation functions in Fig. 5(b) indicates that the hydrogen-bonding network structure of water is weakened along the compression axis, while it is strengthened along the expansion axis. The dynamics of this anisotropic fluctuation of the hydrogen-bonding network structure is coupled with the shear stress, which gives the slowest mode of the viscoelastic relaxation of water.

It should be noted here that our present MD simulation is limited to the ambient temperature. On the other hand, Kawasaki and Kim performed extensive MD simulation of supercooled water, and demonstrated that the temperature dependence of the relaxation time of hydrogen-bonding structure is decoupled from that of the shear relaxation time.⁷ Our theoretical formalism can in principle detect the decoupling predicted by Kawasaki and Kim based on the temperature dependence of the relaxation times, and its application to supercooled water will be an interesting extension of the present work.

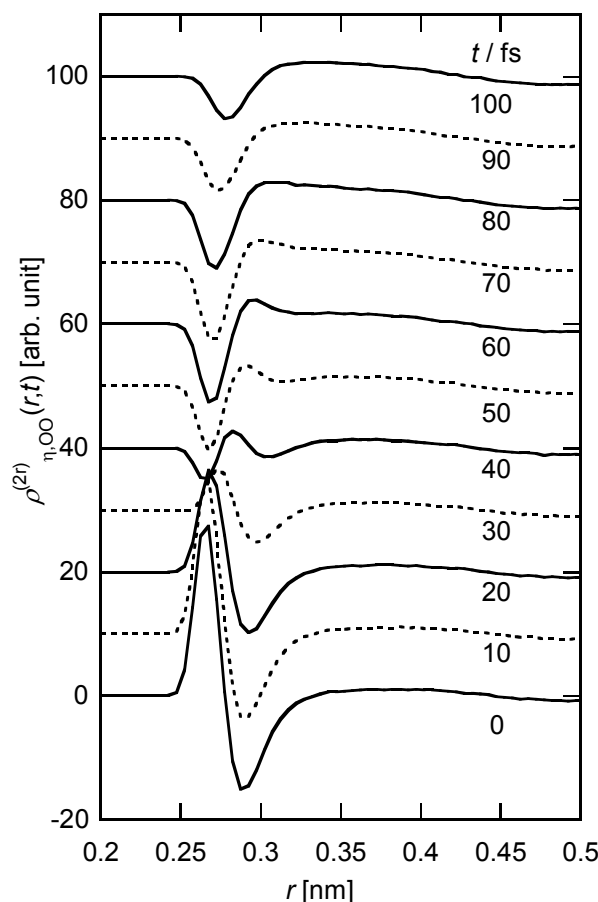


Figure 6. The short-time parts of the cross correlation functions $\rho_{\eta,OO}^{(2r)}(r,t)$ are plotted as the functions of r . The values of the time, t , are exhibited at the right side, and the curves of different values of t are shifted from each other for visibility.

The short-time dynamics of $\rho_{\eta,OO}^{(2r)}(r,t)$ is shown in Fig. 6 in order to analyze the origin of the fast oscillation of $G(t)$ exhibited in Fig. 2(a). Provided that the dynamics is limited almost to the first-peak region of $g_{OO}(r)$, this region is enlarged in Fig. 6.

At the initial time, $t = 0$, a negative peak is observed at $r = 0.27$ nm, the small- r side of the first peak of $g_{OO}(r)$, whereas the positive peak is at $r = 0.29$ nm, the large- r side. The first peak of $g_{OO}(r)$ thus shifts to smaller r along the compression axis at $t = 0$. The amplitudes of the both

peaks decrease with time, and the profile is inverted at $t = 60$ fs, where $G(t)$ shows the first minimum in Fig. 2(a). The inverted profile means that the peak of $g_{OO}(r)$ shifts to *larger-r*. The amplitude of the inverted profile decreases again after 60 fs, and $G(t)$ increases in Fig. 2(a). The fast dynamics shown in Fig. 6 thus describes the oscillation of the O-O distance within the first solvation shell, and the fast oscillation of $G(t)$ in Fig. 2(a) is assigned to the O-O stretching mode. Although the fast oscillation of $G(t)$ may also be explained in terms of the coupling with the collective phonon modes,²³ we consider it is better interpreted as the binary O-O stretching mode because the oscillatory response is limited to the first solvation shell.

It is to be noted here that fast oscillations are often observed in memory functions for the translational diffusion of a solute in solution. We have applied similar analyses for the translational diffusion, and found that the fast oscillation is ascribed to the solute-solvent stretching mode.^{24,25} Given that liquid-state theories have historically been developed on hard-sphere fluids, various memory functions are often understood as the sum of the binary collision and slow relaxation. However, there may be some cases where the fast dynamics is better regarded as the oscillation rather than the collision, particularly when the intermolecular attractive interaction is strong.

The picture on the shear viscosity of liquid water obtained in this work is that it is the anisotropic formation-destruction dynamics of the hydrogen-bonding structure that governs the slow viscoelastic relaxation. Here, we would like to comment on the relation between our present results and the Hall theory on the ultrasonic absorption of liquid water.²⁶ Hall proposed that the bulk viscosity (volume viscosity) of water is assigned to the dynamic equilibrium between the two states, namely, the structured and less-structured ones. The bulk viscosity of liquids is given by the time correlation function of the isotropic part of the stress tensor

1
2
3 according to the Kubo-Green theory. The Hall theory thus implies that the isotropic part of the
4 stress tensor is coupled to the formation-destruction dynamics of the hydrogen-bonding structure.
5
6 Since the anisotropic part of the stress tensor is coupled to the anisotropy of the hydrogen-
7 bonding structure, there is an enough reason to expect that the isotropic part is coupled to the
8 isotropic hydrogen-bonding structure. Therefore, our theory may recover the Hall picture of the
9
10 ultrasonic absorption of water when it is applied to the bulk viscosity, although whether the
11 formation-destruction dynamics of the hydrogen-bonding structure is the two-state equilibrium is
12 a different problem.
13
14
15
16
17
18
19
20

21 The coupling between the hydrogen-bonding structure and the fast heat transfer is another
22 interesting issue. Merabia and coworkers proposed that the fast heat transfer at the interface
23 between metal and water occurs through the viscoelastic mode of water.²⁷ Given that the present
24 work revealed that the viscoelastic relaxation of liquid water is coupled to the hydrogen-bonding
25 structure, the mechanism proposed by them means the fast heat transfer through the hydrogen-
26 bonding network.
27
28
29
30
31
32
33
34
35
36
37
38
39

40 5. Summary

41
42
43

44 The cross correlation function between the shear stress and the two-body density of liquid
45 water was evaluated to clarify the structural origin of shear viscosity. The response of the two-
46 body density to the shear deformation resembles that to the hydrostatic isotropic compression,
47 and it is regarded as the destruction of the hydrogen-bonding structure along the compression
48 axis. Therefore, the shear viscosity of liquid water is ascribed to the anisotropic formation-
49
50
51
52
53
54
55
56
57
58
59
60

destruction dynamics of the hydrogen-bonding structure. The decay rate of the cross-correlation function is approximated fairly well by the square of the intermediate scattering function at the low- q peak of the static structure factor, as is predicted by MCT. The fast oscillatory part of the time-correlation function of the shear stress is assigned to the O-O stretching mode.

AUTHOR INFORMATION

Corresponding Author

E-mail to Tsuyoshi Yamaguchi: yamaguchi.tsuyoshi@material.nagoya-u.ac.jp

ACKNOWLEDGMENT

This work was partly supported by the Japan Society for the Promotion of Science (JSPS), KAKENHI Grant-in-Aid for Scientific Research (C) (No. 16K05514).

REFERENCES

- (1) Bird, R. B.; Stewart, W. E.; Lightfoot, E. N. *Transport Phenomena, 2nd ed.*; John Wiley & Sons: New York, 2007.
- (2) Yamaguchi, T.; Faraone, A. Analysis of Shear Viscosity and Viscoelastic Relaxation of Liquid Methanol Based on Molecular Dynamics Simulation and Mode-Coupling Theory. *J. Chem. Phys.* **2017**, *146*, 244506.

- (3) Kuwajima, K.; Goto, Y.; Hirata, F.; Kataoka, M.; Terazima, M. (eds.) *Water and Biomolecules: Physical Chemistry of Life Phenomena*; Springer: Berlin, Germany, 2009.
- (4) Eisenberg, D.; Kauzmann, W. J. *The Structure and Properties of Water*; Clarendon Press: London, U. K., 1969.
- (5) Yamaguchi, T.; Chong, S.-H.; Hirata, F. Theoretical Study of the Molecular Motion of Liquid Water under High Pressure. *J. Chem. Phys.* **2003**, *119*, 1021–1034.
- (6) Guillaud, E.; Merabia, S.; de Ligny, D.; Joly, L. Decoupling of Viscosity and Relaxation Processes in Supercooled Water: a Molecular Dynamics Study with the TIP4P/2005f Model. *Phys. Chem. Chem. Phys.* **2017**, *19*, 2124–2130.
- (7) Kawasaki, T.; Kim, K. Identifying Time Scales for Violation/Preservation of Stokes-Einstein Relation in Supercooled Water. *Sci. Adv.* **2017**, *3*, e1700399.
- (8) Hansen, J.-P.; McDonald, I. R. *Theory of Simple Liquids, 2nd ed.*; Academic Press: London, U. K., 1986.
- (9) Boon, J.-P.; Yip, S. *Molecular Hydrodynamics*; Dover Publications: New York, 1991.
- (10) Kasahara, K.; Sato, H. Dynamics Theory for Molecular Liquids Based on an Interaction Site Model. *Phys. Chem. Chem. Phys.* **2017**, *19*, 27917–27929.
- (11) Hirata F. (ed.) *Molecular Theory of Solvation*; Kluwer: Dordrecht, Netherland, 2003.
- (12) Abascal, J. L. F.; Vega, C. A General Purpose Model for the Condensed Phases of Water: TIP4P/2005. *J. Chem. Phys.* **2005**, *123*, 234505.

(13) Allen, M. P.; Tildesley, D. J. *Computer Simulation of Liquids*; Clarendon Press; Oxford, U. K., 1987.

(14) Abraham, M. J.; Murtola, T.; Schulz, R.; Pall, S.; Smith, J. C.; Hess, B.; Lindahl, E. GROMACS: High Performance Molecular Simulations through Multi-Level Parallelism from Laptops to Supercomputers. *SoftwareX* **2015**, *1*, 19–25.

(15) Miyamoto, S.; Kollman, P. A. SETTLE: An Analytical Version of the SHAKE and RATTLE Algorithms for Rigid Water Models. *J. Comp. Chem.* **1992**, *13*, 952–962.

(16) Okhulkov, A. V.; Demianets, Yu. N.; Gorbaty, Yu. E. X-Ray Scattering in Liquid Water at Pressures of up to 7.7 kbar: Test of a Fluctuation Model. *J. Chem. Phys.* **1994**, *100*, 1578–1588.

(17) Guevara-Carrion, G.; Vrabec, J.; Hasse, H. Prediction of Self-Diffusion Coefficient and Shear Viscosity of Water and Its Binary Mixtures with Methanol and Ethanol by Molecular Simulation. *J. Chem. Phys.* **2001**, *114*, 074508.

(18) González, M. A.; Abascal, J. L. F. The Shear Viscosity of Rigid Water Models. *J. Chem. Phys.* **2010**, *132*, 096101.

(19) Fanourgakis, G. S.; Medina, J. S.; Prosimi, R. Determining the Bulk Viscosity of Rigid Water Models. *J. Phys. Chem. A* **2012**, *116*, 2564–2570.

(20) Tazi, S.; Boğan, A.; Salanne, M.; Marry, V.; Turq, P.; Rotenberg, B. Diffusion Coefficient and Shear Viscosity of Rigid Water Models. *J. Phys. Cond. Matt.* **2012**, *24*, 284117.

- (21) Mazzacurati, V.; Nucara, A.; Ricci, M. A.; Ruocco, G.; Signorelli, G. High-Resolution Low-Frequency Raman Spectra of Liquid H₂O and D₂O. *J. Chem. Phys.* **1990**, *93*, 7767–7773.
- (22) Ruocco, G.; Sette, F. The High-Frequency Dynamics of Liquid Water. *J. Phys.: Condens. Matter* **1999**, *11*, R259–R293.
- (23) Levashov, V. A. Understanding the Atomic-Level Green-Kubo Stress Correlation Function for a Liquid through Phonons in a Model Crystal. *Phys. Rev. B* **2014**, *90*, 174205.
- (24) Yamaguchi, T.; Matsuoka, T.; Koda, S. Molecular Dynamics Simulation Study on the Transient Response of Solvation Structure during the Translational Diffusion of Solute. *J. Chem. Phys.* **2005**, *122*, 014512.
- (25) Yamaguchi, T.; Matsuoka, T.; Koda, S. Generalized Langevin Theory on the Dynamics of Simple Fluids under External Fields. *J. Chem. Phys.* **2005**, *123*, 034504.
- (26) Hall, L. The Origin of Ultrasonic Absorption in Water. *Phys. Rev.* **1948**, *73*, 775–781
- (27) Marebia, S.; Lombard, J.; Alkurdi, A. Importance of Viscoelastic and Interface Bonding Effects in the Thermal Boundary Conductance of Solid-Water Interfaces. *Int. J. Heat Mass Transfer* **2016**, *100*, 287–294.

TOC Graphics

